

Carbon Nanofiber Based Films for Anti-icing/Anti-frosting Applications

BY

SHREYAS KAPATRAL

B.Tech (National Institute of Technology, Rourkela) 2008

THESIS

Submitted in partial fulfillment of the requirements
for the degree of Master of Science in Mechanical Engineering
in the Graduate College of the
University of Illinois at Chicago, 2013

Chicago, Illinois

Defense Committee:

Constantine M. Megaridis, Chair and Advisor

Amin Salehi-Khojin

Ranjan Ganguly, Power Engineering Department, Jadavpur University

Copyright by
Shreyas Kapatral
2013

This thesis is dedicated to my parents.

ACKNOWLEDGMENTS

I would like to sincerely thank my advisor Prof. Constantine M. Megaridis for his guidance and support throughout my graduate studies. He truly changes the way one looks at a problem, adding a new perspective and approach to it. I would like to thank Arindam Das and Thomas Schutzius, who introduced me to the topic of wettability and equipped me with valuable experimental techniques. Special thanks to Thomas Schutzius and Dr. Ranjan Ganguly for their valuable technical inputs and discussions. I would like to thank Dr. Ranjan Ganguly and Dr. Amin Salehi-Khojin for serving on my thesis committee. I would like to acknowledge all the help and fun-filled moments spent with my labmates Joseph, Aritra, Ramsey and Mohamed. I am really thankful to Eric, Dave and Sandy at the UIC machine shop for their contributions in the experimental setup, they put together a great contraption. Lastly, I would like to thank my family here, in Chicago and back home for their immense love and support.

TABLE OF CONTENTS

<u>CHAPTER</u>		<u>PAGE</u>
1	INTRODUCTION	1
1.1	Brief Theoretical Background	5
2	CONDENSATION	7
2.1	Introduction	7
2.2	Experimental	8
2.2.1	Materials and Methods	8
2.2.2	Wettability Characterization	9
2.2.3	Condensation	9
2.3	Results and Discussion	10
3	FROSTING AND DEFROSTING	17
3.1	Experimental	18
3.1.1	Materials and Methods	18
3.1.2	Electrical Resistance and Temperature Measurement	18
3.1.3	Condensation Frosting	19
3.2	Results and Discussion	19
3.2.1	Coating wettability and heating performance	19
3.2.2	Condensation Frosting and Defrosting by Joule Heating	24
4	CONCLUSION	31
	CITED LITERATURE	33
	VITA	38

LIST OF TABLES

<u>TABLE</u>		<u>PAGE</u>
I	WETTABILITY DATA FOR DIFFERENT COMPOSITIONS OF CNF-PMC COATINGS.	12
II	COMPARISON OF THE HEATING PERFORMANCE OF NANOCARBON- BASED HEATERS FROM LITERATURE.	22

LIST OF FIGURES

<u>FIGURE</u>		<u>PAGE</u>
1	(a) Equilibrium contact angle of a droplet with balancing surface energies at the three phase line. (b) Droplet on a hydrophilic surface in a Wenzel state. (c) Droplet sitting on a composite surface in a Cassie state.	6
2	Schematic of the experimental setup to study the condensation characteristics of nanocomposites. Note: α is the angle of inclination.	10
3	Scanning electron micrographs showing the morphology of varying compositions of CNF-PMC spray cast composite films on glass (a) 20 wt.% CNF (b) 30 wt.% CNF and (c) 50 wt.% CNF in the solid composite. (d), (e) and (f) show higher magnification images of (a), (b) and (c) respectively. The zoomed out images show coverage of the polymer matrix in the CNF web.	11
4	Time evolution of droplet condensation, (a) 30 min and (b) 60 min from the time of cooling. (c) Nanocomposite surface immediately after a droplet shedding event. (d) Time evolution of condensates 10 min after droplet shedding event in (c). Images (c) and (d) are captured over the same sample area. Note: The bright rings observed on the droplet are reflections of the light source.	14
5	Images captured immediately after a droplet shedding event on (a) 20 wt.%, (b) 30 wt.% and (c) 50 wt.% CNF coatings. The highlights show wetted regions or spots.	15
6	Different condensate morphologies: (a) wetted, (b) partially wetted, and (c) suspended states on hypothetical nanostructured surface.	15
7	SEM images of superhydrophobic and conductive CNF-PMC spray cast coating (50 wt.% CNF weight in the solid coating) with increasing magnification from (a) to (b). The inset in (b) shows a sessile $7\mu\text{L}$ droplet on the CNF-PMC film in a superhydrophobic state ($\text{CA} = 155^\circ$) induced by the re-entrant nature of the entangled CNFs held together by the PMC.	20
8	(a) Stepwise process of depositing electrodes on the dry CNF-PMC coating on glass slide (7.5×2.5 cm). (b) Schematic of the setup electrothermal characterization.	21

LIST OF FIGURES (Continued)

<u>FIGURE</u>		<u>PAGE</u>
9	(a) Reduction in sheet resistance with amount of solid CNF-PMC coating deposited on the glass substrate. (b) I-V characteristics of the CNF-PMC coatings with varying sheet resistance (coating thickness). (c) Temperature evolution of a 110 Ω CNF-PMC coating for various values of applied DC voltage. (d) Steady state temperature versus input power density for the same coating as in (c).	23
10	Image sequence showing out-of-plane droplet jumping. Two clusters of droplets below 50 μ m are encircled in red in (a) in their pre-coalescence state (1,2). In (b), the droplets in the red area are still distinct (2), while those in the yellow area have coalesced and departed out of the surface leaving behind pristine sites for fresh nucleation to occur thereby (1'). In (c), both areas are devoid of droplets and start a new cycle of liquid nucleation (1',2').	25
11	Stages of frost growth. The condensed supercooled droplets froze, frost preferentially grew on the tip of the droplets forming a porous dendritic structure.	26
12	Surfaces (a) glass slide, (b) 50 wt.% CNF coating and (c) 50 wt.% CNF coating with joule heating after exposure to humid ambient (15°C and RH = 80%) for 1 hour. Surfaces (d) glass slide and (e) 50 wt.% CNF coating still covered with frost and (f) 50 wt.% CNF completely frost free after application of 40V DC for 70s. (g) Sequence of images showing rapid transition of frosted coating (c) to completely ice free surface (f) by joule heating. Each image in sequence (g) is captured 10s apart. . .	27
13	Top view of dynamic defrosting by skin heating. A constant DC voltage of 40V was applied to the coating till the coating became frost free. The temperature of the coating rose from -10°C to just above melting point (\sim 2°C), eventually leaving a frost-free surface. Time was set to zero from the point of application of the voltage.	29
14	Side view images showing dynamic defrosting at low angle of inclination of $\alpha = 10^\circ$ in humid environment (ambient temperature of 15°C and RH of 80%).	30
15	Illustration of dynamic defrosting. (a) Porous frost formed on the frozen condensates in a Cassie state, (b) Melted droplets absorbed by the porous medium. The frost layer fractures carrying partially melted solid-liquid mixture. (c) The sheet of solid-liquid mixture either curls away or forms a droplet that rolls away leaving a frost-free surface.	30

LIST OF ABBREVIATIONS

CA	contact angle
CAH	contact angle hysteresis
CNF	carbon nanofiber
CNT	carbon nanotube
DWC	dropwise condensation
IFE	interfacial free energy
LIS	liquid infused surface
MWCNT	multi-walled carbon nanotube
PMC	fluoroacrylic copolymer
SSD	supersaturation degree
SWCNT	single-walled carbon nanotube
RH	relative humidity

SUMMARY

Superhydrophobic surfaces have been extensively studied for mitigating the icing problem. Recent investigations concluded that superior anti-icing surfaces must engender excellent anti-frosting and efficient defrosting properties. In the present study, carbon nanofiber based water repellent polymeric composites were investigated for anti-icing/anti-frosting applications. Use of low cost, off-the-shelf materials, simple solvent based processing and spray casting enhance substrate independence and scalability of the nanocomposites. The first half of the thesis is devoted towards tuning the nanoscale surface texture to attain sustained DWC. Complete removal of ice accumulated by condensation frosting was shown to have significant dependence on condensate morphology prior to freezing. In the latter half of this work, the self-heating capability of the electrically conductive coating was utilized to demonstrate dynamic defrosting at very low substrate inclination angles. The mechanism behind facile dewetting of the frost layer was discussed. We focused on the synergetic combination of electrothermal deicing and superior water repellency to reduce energy, time and cost required to keep a surface ice-free.

CHAPTER 1

INTRODUCTION

Ice accumulation and frosting are ubiquitous at high altitudes, cold regions and humid environments. The pervasive nature of ice and frost at low temperatures is detrimental to the functionality and performance of man-made equipment and systems like aircraft, off-shore structures, wind turbines, power lines, telecommunication equipment and heat exchangers [1–6]. Recently, there has been increased interest in developing surfaces that retard and reduce frost/ice formation and adhesion. One dominant approach is the use of bio-inspired micro/nano structured superhydrophobic surfaces with high water contact angle ($CA > 150^\circ$) and low contact angle hysteresis ($CAH < 10^\circ$) [7]. Superhydrophobic surfaces show delay in ice nucleation and frosting by reducing the effective surface area available for heat transfer at the droplet interface, increasing the energy barrier for nucleation, and facilitating droplet coalescence, shedding or jumping [8,9]. These surfaces also prevent and minimize ice accumulation in dynamic situations involving supercooled droplet impact in freezing rain conditions [10,11]. However, a recent study has brought to question the emphasis on super water-repellent surface formulations for ice formation/retardation and suggested that anti-icing design must optimize the competing influences of both wettability and roughness [12]. The water repellent and anti-icing properties of superhydrophobic surfaces are severely compromised when they are exposed to high humidity frosting conditions [13,14]. Some studies also show that ice/frost on superhydrophobic surfaces form in an impaled Wenzel state, thereby enhancing the adhesion by anchoring to the surface

roughness, which increases the energy and time required for ice/frost removal [15]. The other approach is the use of liquid infused surfaces (LIS) which rely on low contact angle hysteresis to shed small droplets before freezing on the surface. The performance of LIS is limited by oil drainage caused by capillary forces arising from dendritic frost formed on the frozen droplet and from cloaking [16, 17]. Further, LIS need very careful design of the surface texture-oil pair or an external source of oil to retain/replenish the depleting lubricating liquid on these surfaces when exposed to repeated frosting-defrosting cycles. Above discussed approaches are passive as they solely rely on surface roughness and wettability to mitigate icing.

Despite extensive research on passive approaches, frosting on superhydrophobic surfaces is unavoidable over prolonged freezing periods due to edge effects, surface defects and external disturbances (or forces) which could cause local reduction in energy barrier causing heterogeneous or homogeneous nucleation, thereby initiating a propagating freezing wave leading to frosting of the entire surface [18, 19]. Hence there is high demand for developing surfaces which not only passively delay ice formation, but also actively mitigate/eliminate ice formation/accumulation and even remove ice/frost when formed.

Due to high water CA on hydrophobic surfaces, the critical Gibbs energy required for phase change is higher in the case of desublimation than for condensation frosting. The critical supersaturation degree (SSD_{cr}) required for desublimation on a surface with water $CA \approx 160^\circ$ is almost three times greater than the SSD_{cr} required for condensation frosting [20]. Thus, condensation frosting is the most prominent mode of phase change on hydrophobic surfaces, and thus far more relevant to practical applications. Very few condensation frosting studies have

been performed on superhydrophobic surfaces which, when defrosted by raising surface temperature, demonstrate complete dewetting and roll-off of partially melted frost from the surface at very low tilt angles ($\alpha \approx 10^\circ$). This is known as dynamic defrosting, and was first observed on rigid hierarchical superhydrophobic surfaces at large inclinations ($\alpha = 90^\circ$) [21]. During condensation frosting, nanostructured superhydrophobic surfaces promote droplet condensation in a Cassie state; the frost which grows on these frozen condensates assumes a Cassie state, having very low contact area, and hence lower adhesion. Dynamic defrosting (at $\alpha \approx 0^\circ$) on nanostructured surfaces is attributed to the thermodynamically driven minimization of surface energy of the water in the melted slush, resulting in a mobile water-ice mixture having low CAH [9]. In addition to forming Cassie frost, hierarchical micro/nanostructured superhydrophobic surfaces leverage on the microscale roughness to enable complete dewetting and enhance mobility of the melted frost by providing a composite lubricating air layer. Dynamic defrosting reduces the time, energy and force required for frost removal; therefore this capability is required for efficient antifrosting surfaces [22].

We report spray-deposited, electrically-conductive and superhydrophobic, nanocomposite coatings that can actively mitigate condensation frosting on demand. There has been extensive research in electrothermal methods which utilize the Joule heating effect by passing electrical current through conductors for ice removal; however, none of these studies have reported self-heating, superhydrophobic, carbon-nanomaterial-based polymeric coatings as an active approach to address the icing problem. Superhydrophobic surfaces can reduce the energy required to prevent ice accretion by 80% by adding heat from underneath using external devices or sys-

tems [23]. Our conductive superhydrophobic coating doubles up as the heating element itself (skin heating), which makes its action more effective because heat is added where it is most needed (at the surface/ice interface), thus making it easier to partially melt and dislodge the ice. The coating saves cost, weight, space and energy by eliminating the need for external heating elements or systems and locally heating only the ice-coating interface instead of the substrate itself. In this study, we spray deposit solution based fluoroacrylic-carbon nanofiber (CNF) dispersions on insulating glass slides to form conductive superhydrophobic coatings [24]. The sheet resistance (R_s) of the coating is quantified with respect to increasing add-on deposition levels on the substrate. The heating performance of the CNF coating is characterized based on the applied DC voltage and compared with nanocarbon-based film heaters reported in the literature. Condensation frosting is studied on these surfaces and skin heating is employed to demonstrate dynamic defrosting at low tilt angles ($\alpha = 10^\circ$) and high relative humidity (RH). The present coatings add a new dimension to existing surface technologies combining passive anti-ice approaches with active removal techniques, such as electrothermal and/or mechanical methods, to reduce the energy cost for ice avoidance. The coatings offer a facile, scalable, substrate- and geometry-independent approach for developing functional materials with superior anti-icing properties.

1.1 Brief Theoretical Background

Wettability of a solid interface depends on its surface free energy and texture (roughness). For a smooth chemically homogeneous surface the equilibrium contact angle (θ_E) is given by the Young's relation (Figure 1) [25]

$$\theta_E = \frac{\gamma_{sv} - \gamma_{sl}}{\gamma_{lv}} \quad (1.1)$$

where γ_{sv} , γ_{sl} and γ_{lv} are the interfacial surface energies of the solid-vapor, solid-liquid and liquid-vapor phases respectively. Roughness further amplifies the wettability of a surface, making a hydrophilic surface more hydrophilic and a hydrophobic surface more hydrophobic. The Wenzel model relates the apparent contact angle (θ_W^*) to θ_E by the ratio of actual surface area to the apparent surface area, r [26]. In such situations the liquid impales the roughness features as shown in Figure 1b. The apparent contact angle is given by

$$\cos\theta_W^* = r\cos\theta_E \quad (1.2)$$

In cases where a droplet rests on a chemically heterogeneous surface the Cassie-Baxter model applies [27]. On rough hydrophobic surfaces liquid is in contact with a composite interface constituting air pockets trapped within the surface texture and the liquid interface (Figure 1c). The apparent contact angle (θ_C^*) of a composite surface is related to θ_E by considering the contributions from the individual solid and gas interfacial energies given by

$$\cos\theta_C^* = \phi_S(\cos\theta_E + 1) - 1 \quad (1.3)$$

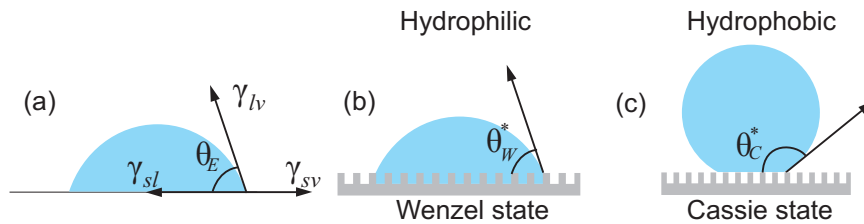


Figure 1. (a) Equilibrium contact angle of a droplet with balancing surface energies at the three phase line. (b) Droplet on an hydrophilic surface in a Wenzel state. (c) Droplet sitting on a composite surface in a Cassie state.

where ϕ_S is the fraction of solid area in contact with the droplet. The mobility of a droplet on a surface is characterized by the contact angle hysteresis (CAH), the difference between the advancing contact angle (θ_a^*) and receding contact angle (θ_r^*). Lower CAH is desired for easy droplet roll-off and coalescence during condensation. Facile droplet mobility delays condensation frosting and reduces ice accretion by facilitating departure of smaller droplets before they can freeze on the surface [23, 28]. Though Wenzel and Cassie-Baxter theories satisfactorily explain the wetting properties of a surface for a deposited droplet, they only provide an indication of the state a microscale droplet would assume after nucleation and/or coalescence during phase change [29].

CHAPTER 2

CONDENSATION

2.1 Introduction

Dropwise condensation (DWC) shows many folds increase in heat transfer rates than film-wise condensation [30]. The wettability of a surface significantly affects the heat transfer coefficient. Superhydrophobic surfaces enhance the DWC heat transfer rate by limiting the maximum size of condensate departure from the surface by droplet sliding and/or jumping [31, 32]. Thus, surfaces with superhydrophobic properties have been increasingly studied to promote DWC. Condensates formed on a superhydrophobic surfaces assume either wetted (W), partially wetted (PW) and/or suspended (S) states [33–36]. PW droplets locally wet the surface between the nanoscale features still maintaining a high contact angle whereas, spherical S droplets rest on composite solid-air interface. Nanoscale roughness and nucleation density dictate the condensate morphology and droplet growth [29, 37]. The final wetting state of the micro-droplets is thermodynamically governed by attainment of minimum interfacial free energy (IFE) while a condensate dewets the surface texture (decreasing base radius) [38]. PW droplets are desired over S morphology to enhance heat transfer [39]. The contact area of the PW droplets is larger leading to faster growth rates while maintaining droplet mobility. In contrast, for applications in anti-icing/anti-frosting the superhydrophobic surfaces must be designed to realize S droplet

morphology, limiting the solid-liquid surface area causing delay in freezing and facilitating easy droplet roll-off.

In the present work we first study the condensation characteristics of the nanocomposite coatings as a precursor to its frosting/anti-frosting behavior. The filler to polymer ratio in the nanocomposite is varied to tune the nanoscale roughness thus influencing condensate morphology. Optimal filler concentration (50 wt.% CNF in the solid coating) is identified to ensue DWC. Sustained DWC is demonstrated at 13°C and high relative humidity (RH = 70%) on the 50 wt.% CNF coating. Effective defrosting on a surface is shown to be strongly influenced by the droplet morphology and subsequent growth before condensation frosting.

2.2 Experimental

2.2.1 Materials and Methods

The first step comprised CNF (PR-24-XT-HHT; Pyrograf III, Applied Science Inc.,USA) treatment with diluted acetic acid (ACS reagent, ≥ 99.5 wt.%, Sigma Aldrich) solution (1:2 wt. ratio in acetone). The CNF dispersion (0.75 wt.% in acid and acetone) was then stabilized by probe sonication (750 W, 13 mm probe dia., 40% amplitude, 20 KHz frequency, Sonics and Materials, Inc., Model VCX-750) for 1.5 min. In another vial, fluoroacrylic copolymer (PMC, 20 wt.% in water, Capstone[®] ST-100, DuPont) was diluted with acetic acid and acetone (1:2 wt. ratio) to form a 5 wt.% PMC solution. This solution was then mixed with the CNF dispersion in different proportions to create 20 wt.%, 30 wt.% and 50 wt.% CNF (wt.% CNF in the dried solid CNF-PMC nanocomposite) which was bath sonicated (Cole Palmer, Model 8821) for 10 minutes to form a ready-to-spray fluid. The final dispersion was then sprayed on

glass slides ($7.5 \times 2.5 \times 0.1 \text{ cm}^3$) using an air brush (Paasche, VL-Set Siphon feed, 0.73 mm spray nozzle, at 15 psi (≈ 0.1 bar gauge pressure) from a distance ≈ 5 cm and dried at 90°C in a convective oven for half an hour to completely vaporize the solvents.

2.2.2 Wettability Characterization

Water (deionized) contact angle and contact angle hysteresis was measured by placing sessile $7\mu\text{L}$ water droplets on the coating; recorded by high speed camera (Redlake Motionpro) at 60 fps. For every new measurement, droplets were placed on a different location on the coating and five measurements were made to produce each value. All wettability measurements were made at room temperature.

2.2.3 Condensation

The condensation experiments were performed in a temperature- and humidity-controlled environmental chamber (Espec, SH641) at constant ambient temperature of 13°C and high relative humidity $\text{RH} = 70\%$. Figure 2 shows a schematic of the experimental setup. Humidity of the chamber was monitored by an environmental meter (Aktakom ATE-9538). Peltier cooler (Tetechnology, Inc., CP061) was used to heat/cool the surface temperature of the test coatings independent of the chamber temperature. The coating was held at a constant temperature of $2 \pm 1^\circ\text{C}$. Thermally conductive glue (Omegatherm 201) was used to paste the samples on the peltier stage. The temperature of the coatings was measured using T-type thermocouples and recorded using a data acquisition system (DAQ, Omega, 2400 series) at 5 Hz. All images reported were extracted from real time video recorded using a CCD camera (Pulnix) with zoom

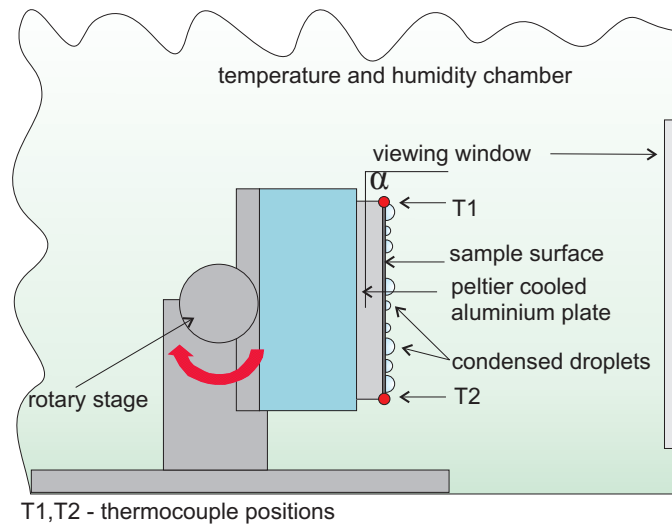


Figure 2. Schematic of the experimental setup to study the condensation characteristics of nanocomposites. Note: α is the angle of inclination.

lens (Optem 100). All tests were performed for a duration of two hours from when the coatings reached the desired temperature.

2.3 Results and Discussion

We spray deposited the CNF-PMC dispersion on glass slides to form films of varying wettability. The CNFs (diameter ≈ 100 nm, length $\approx 50 - 100$ μm after probe sonication) impart texture required to achieve superhydrophobicity. PMC not only provides low surface energy and improved substrate adhesion but also helps in dispersing and stabilizing the CNFs in the solvent system [24]. The surface morphology of CNF-PMC coatings for increasing CNF loading is shown in the Figure 3. The surfaces appear to be made of similar randomly distributed microscale features (Figure 3). Table I lists the wettability properties of CNF-PMC coatings

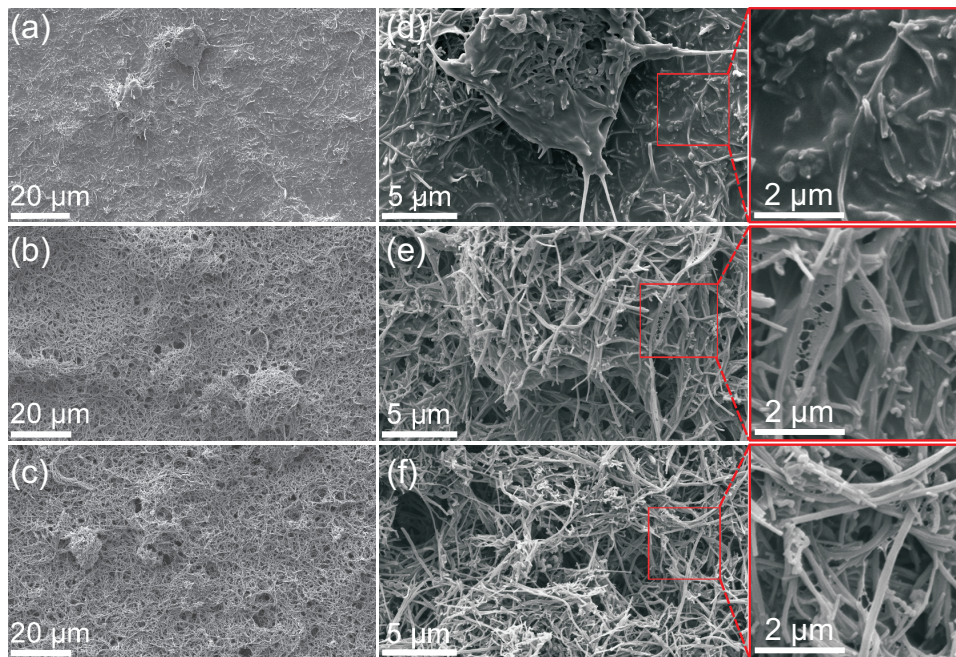


Figure 3. Scanning electron micrographs showing the morphology of varying compositions of CNF-PMC spray cast composite films on glass (a) 20 wt.% CNF (b) 30 wt.% CNF and (c) 50 wt.% CNF in the solid composite. (d), (e) and (f) show higher magnification images of (a), (b) and (c) respectively. The zoomed out images show coverage of the polymer matrix in the CNF web.

with increasing CNF wt.% of the dried solid coating. As the filler loading increased the surfaces became more hydrophobic, showing a transition from hydrophobic, 20 wt.% CNF coating with ($\theta^* < 150^\circ$) to superhydrophobic and selfcleaning 50 wt.% CNF coating ($\theta^* > 150^\circ$ and $CAH < 10^\circ$). The transition from hydrophobicity to superhydrophobicity occurred at CNF loading of 30 wt.%. Sessile droplets deposited on 20 wt.% CNF coating remained stuck even when the surface was placed vertically. The 20 wt.% CNF coating forms a sticky hydrophobic surface indicated by the high apparent contact angle (θ^*) and very low receding angle (θ_r^*) (Table I).

TABLE I

WETTABILITY DATA FOR DIFFERENT COMPOSITIONS OF CNF-PMC COATINGS.

Composition	Contact angle	Advancing contact angle	Receding contact angle	Contact angle hysteresis
20 wt.% CNF	$141^\circ \pm 4^\circ$	$166^\circ \pm 1^\circ$	$\approx 0^\circ$	S ^a
30 wt.% CNF	$159^\circ \pm 2^\circ$	$168^\circ \pm 2^\circ$	$150^\circ \pm 2^\circ$	$18^\circ \pm 3^\circ$
50 wt.% CNF	$163^\circ \pm 2^\circ$	$169^\circ \pm 2^\circ$	$157^\circ \pm 1^\circ$	$11^\circ \pm 2^\circ$

^aS indicates that the droplet remained stuck to the surface.

Higher magnifications of the SEM micrographs reveal visible differences in nanoscale features. Figure 3d is the zoomed out image of 20 wt.% CNF coating showing randomly distributed CNFs forming a mesh like structure immersed in the polymer matrix exposing only slightly the curved features of the CNF mesh. Whereas, magnified image of the 50 wt.% CNF coating (Figure 3f) shows three dimensional porous structure of the CNF mesh of varying pore sizes. These pores are formed by highly reentrant features of the CNFs favouring thermodynamically stable liquid-solid interface [40]. The reentrant texture formed by the CNF mesh enable the composite films to repel low surface tension liquids like oils [41]. Superoleophobicity is highly desirable to prevent loss of water repellency due to external contamination. The polymer forms interconnecting webs between the porous CNF structure for 30 wt.% CNF loading.

Droplets nucleated at random locations during the initial phase of condensation. The droplets remained stationary as they grew, until they coalesced with neighbouring droplets forming larger condensates. The droplet morphology for first 30 min of condensation is observed in Figure 4. The condensates on 20 wt.% CNF coating are in Wenzel state causing

the surface to appear dark. The wetted droplets remained immobile even after merging with neighbouring droplets as seen after 60 min of condensation, until they grew large enough to be shed by gravity (Figure 4). The contact line of the wetted droplets remained pinned to the surface significantly reducing the droplet mobility. The droplets on 30 wt.% and 50 wt.% CNF coatings appeared spherical in shape. These droplets appear shiny from the light reflected from the air pockets trapped between the liquid-solid interface suggesting the droplets assume a Cassie state. Droplets on the superhydrophobic surfaces moved rapidly on merging with neighbouring droplets, opening fresh sites for nucleation (Figure 4b). These merging events were more frequent on the 50 wt.% CNF coating showing higher droplet mobility and lower surface adhesion of the condensates. Although the droplets on the 30 wt.% CNF coating remained spherical in shape they showed limited droplet mobility.

After ~ 60 min, the droplets grew large (few mm in diameter) enough to be acted upon by gravity, triggering droplet shedding. Surfaces immediately after such a shedding event is shown in Figure 4c. A thin liquid film is left behind a shedding droplet on the 20 wt.% coating. Such a thin liquid film is undesirable as it adds to the thermal resistance decreasing the overall heat and mass transfer. Further, the liquid film entirely covers the surface inhibiting DWC, Figure 4d shows the surface still covered by the liquid film 10 min after the shedding event. Shedding droplets cleared up fresh nucleating sites on 30 wt.% and 50 wt. % CNF coatings (Figure 4c). The superhydrophobic surfaces were rejuvenated with new condensates which grew (Figure 4d), merged and departed from the surface repeating the growth-shedding cycle. Figure 5 clearly shows the wetted regions or spots after a droplet shedding event. Wetted spots on the 30 wt.%

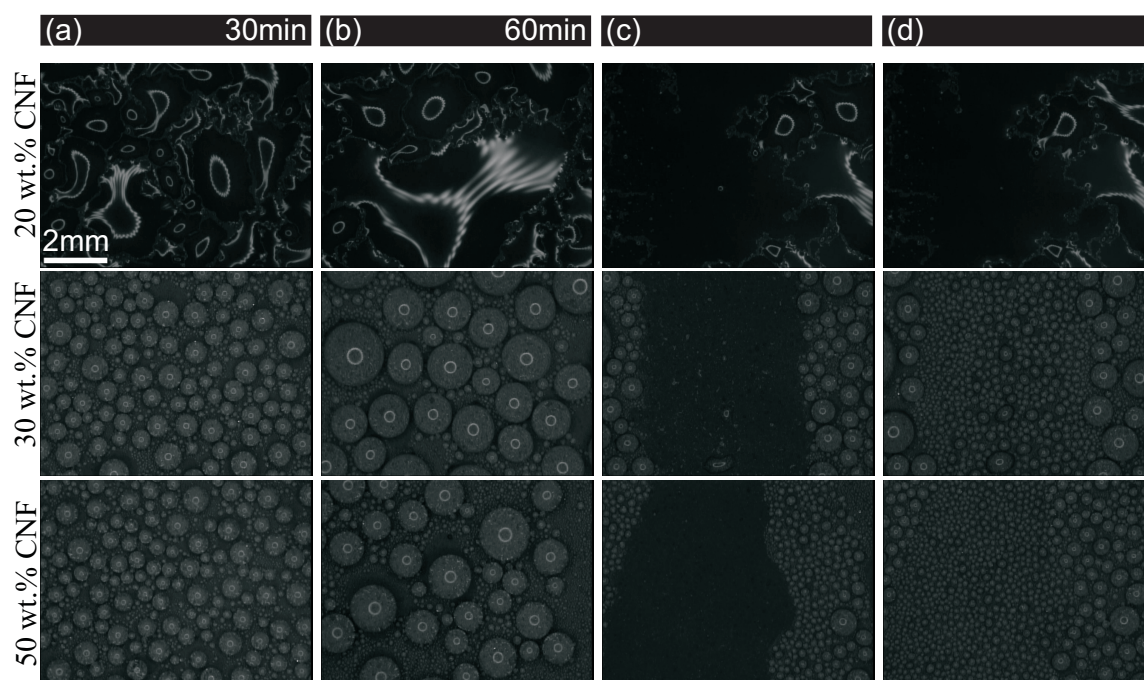


Figure 4. Time evolution of droplet condensation, (a) 30 min and (b) 60 min from the time of cooling. (c) Nanocomposite surface immediately after a droplet shedding event. (d) Time evolution of condensates 10 min after droplet shedding event in (c). Images (c) and (d) are captured over the same sample area. Note: The bright rings observed on the droplet are reflections of the light source.

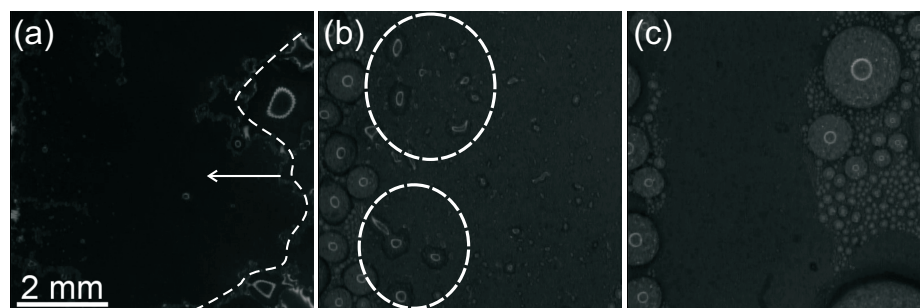


Figure 5. Images captured immediately after a droplet shedding event on (a) 20 wt.%, (b) 30 wt.% and (c) 50 wt.% CNF coatings. The highlights show wetted regions or spots.

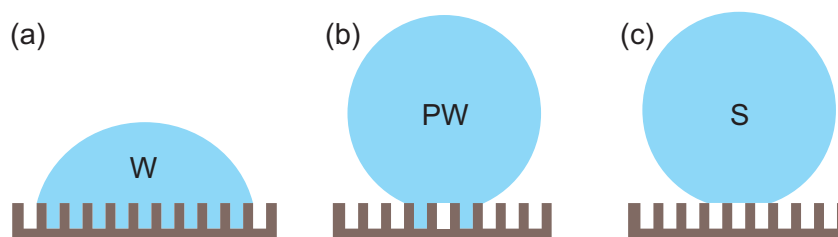


Figure 6. Different condensate morphologies: (a) wetted, (b) partially wetted, and (c) suspended states on hypothetical nanostructured surface.

coating suggest that the condensates assume PW morphology. 50 wt.% CNF-PMC coating showed sustained DWC indicating a mobile S condensate morphology (Figure 6). Increased droplet mobility leads to larger number of merging events, this is highly desirable as merging events can cause transition from PW to S state [29,42]. The average diameter of the departing droplets for 10 such shedding events were recorded. The average macroscopic droplet shedding diameter on 30 wt.% CNF coatings was 3.2 ± 0.5 mm and on 50 wt.% coating was 2.5 ± 0.4 mm. The droplet shedding diameter on 50 wt.% coating is comparable to the capillary length (≈ 2.7 mm), almost $\sim 30\%$ smaller than average droplet shedding size of 30 wt.% coating. Larger CAH causes contact line pinning and the partially wetted spots lead to larger sliding droplets on the 30 wt.% CNF coating as compared to the 50 wt.% coating. 50 wt.% CNF coating showed supreme performance under condensation.

Nanoscale texture influences the condensate morphology. Smaller droplet shedding diameters correspond to lower CAH. Lower CAH is highly desirable to facilitate sliding/shedding of smaller droplets before freezing on the surface preventing icing. Residual liquid films or wetted spots after shedding compromise the wettability of the surface, acting as preferred sites for ice nucleation or frosting. Efficient shedding is attained when a surface is tuned to promote S condensates. Growth rate of S condensates is lower than PW condensates [39]. Hence, under condensation frosting a surface promoting suspended condensates will have smaller droplets with reduced liquid-solid contact area forming Cassie frost.

CHAPTER 3

FROSTING AND DEFROSTING

Nanostructured superhydrophobic surfaces show significant delay in frosting *i.e.*, the condensed micro-droplets remain in a liquid state below freezing temperatures for longer durations. Condensates on superhydrophobic surfaces assume high contact angle similar to deposited sessile droplets at room temperature thereby, increasing the free-energy barrier for heterogeneous nucleation [43–45]. High contact angles indicate that the droplets rest on a composite (solid-air) interface, the air layer decreases the overall heat exchange between the droplet and the surface providing insulation thus, delaying solidification [46]. Increased droplet mobility owing to low CAH of superhydrophobic surfaces facilitate jumping-droplets, where the excess surface energy released upon droplet merging, impart enough kinetic energy for out-of-plane droplet departure, further delaying freezing [35,47]. Though superhydrophobic surfaces manifest frosting delay and suppress frost growth they cannot completely eliminate frost formation. Frost or condensates compromise the wettability of the surface rendering it useless in icing conditions; also, increasing the ice adhesion [13]. Hence, robust anti-icing surfaces must be superior anti-frosting surfaces facilitating efficient defrosting. Having identified an optimal composition to promote DWC (chapter 1), we next investigate the condensation frosting performance of the 50 wt.% CNF coatings. Very few studies have been performed on surfaces which show complete dewetting of the melted frost from the surface at relatively low inclination angles (called dynamic defrosting) [9, 22]. Dynamic defrosting reduces the time, energy and gravi-

tational force required for deicing. CNFs not only impart surface texture required for robust superhydrophobicity but also bear the nanocomposite electrical conductivity. In the present study the temperature of the coating is raised by passing current through the conductive coating (*i.e.*, joule heating effect) to actively mitigate ice formation. The electrothermal response of the self-heating superhydrophobic coating is characterized and its heating performance is compared to nanocarbon based heaters reported in the literature. Dynamic defrosting by skin heating is demonstrated as an active electrothermal approach to keep the coating ice-free. Heat is applied locally (ice-surface interface), minimizing energy loss and time spent in rising substrate temperature.

3.1 Experimental

3.1.1 Materials and Methods

Same procedure was followed as reported in section 2.2.1 to spray cast 50 wt.% CNF-PMC coating on glass slides.

3.1.2 Electrical Resistance and Temperature Measurement

Electrodes were deposited on the dried coatings by first applying highly conductive silver paste (Ted Pella, Inc., Pelco colloidal liquid) and pasting conductive Cu tape (McMaster-Carr) once the silver paste was dried (Figure 7a). The resistance of the coating was measured by four probe measurement technique using a digital multimeter (Agilent 34401a). The I-V characteristics were determined by an electrometer (Keithley 6517) with an variable DC voltage source (Keithley 230). The heating performance of the coatings was measured by applying constant DC voltage (Sorensen DCR 40-13B). The real time temperature evolution of the

coatings was measured by T-type thermocouples (locations of thermocouples on the coating is shown in Figure 7b) using a data acquisition system (DAQ, Omega, 2400 series) at 5 Hz. Temperature evolution measurements were made in well controlled environment of 20°C in a temperature- and humidity- controlled environmental chamber (Espec, SH641).

3.1.3 Condensation Frosting

The condensation frosting experiments were performed in the setup as described in section 2.3.3. The chamber is maintained at a constant ambient temperature of 15°C and high relative humidity RH = 80%. For every test, the coating was cooled at a steady rate of $\sim 3^\circ\text{C}/\text{min}$ from the ambient temperature to a constant temperature of $-10 \pm 1^\circ\text{C}$. Such a low cooling rate was chosen to ensure that condensation was the prominent phase change mechanism followed by frosting. Frost was allowed to accumulate for 1 hour from the onset of cooling. To study dynamic defrosting, a constant DC voltage (Sorensen DCR 40-13B) was applied across the coating until the coating was completely frost-free.

3.2 Results and Discussion

3.2.1 Coating wettability and heating performance

We spray deposited CNFs in a fluoroacrylic co-polymer (PMC) matrix on glass slides to form superhydrophobic and self-cleaning films. PMC provides low surface tension and good substrate adhesion, while CNFs provide hierarchical micro/nano scale surface texture and electrical conductivity when deposited in concentrations well above percolation [48]. Figure 7 shows distinct microscale features formed by the CNF network with highly re-entrant cylindrical geometry in a mesh-like configuration. This combination of low surface energy and hierarchical roughness

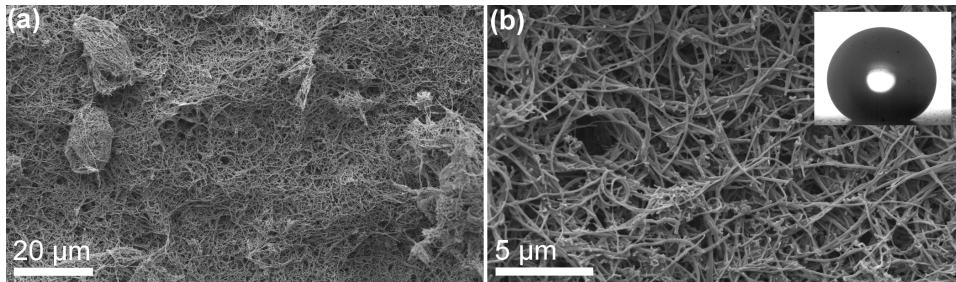


Figure 7. SEM images of superhydrophobic and conductive CNF-PMC spray cast coating (50 wt.% CNF weight in the solid coating) with increasing magnification from (a) to (b). The inset in (b) shows a sessile $7\mu\text{L}$ droplet on the CNF-PMC film in a superhydrophobic state ($\text{CA} = 155^\circ$) induced by the re-entrant nature of the entangled CNFs held together by the PMC.

leads to high water CA of $155^\circ \pm 2^\circ$ and low CAH of $5^\circ \pm 3^\circ$ (rollover angle $< 10^\circ$) measured with sessile $7\mu\text{L}$ droplets at room temperature and 40% RH.

We characterized the heating performance of the coatings with applied DC voltage. Figure 8a shows the step-wise sample assembly process of first depositing electrically conductive Ag paste and then Cu tape to form low resistance electrodes at the edges of the coated slides. Lower electrical contact resistance at the electrodes improves the heating performance, which is facilitated by the layer of silver paste. The resistance of the coating was measured using the four probe measurement technique and varied from 576 - 73 Ω . The sheet resistance of the coating (Figure 9a) decreased from 180 $\Omega \text{ sq}^{-1}$ to 24 $\Omega \text{ sq}^{-1}$ as solid mass deposited on the glass slide increased; the coating buildup was achieved by multiple spray passes over the same area. The lowest sheet resistance corresponded to the highest coating add-on level of $\sim 11.5 \text{ gm}^{-2}$. The smaller error bars of the resistance measurement for higher coating add-on levels indicate

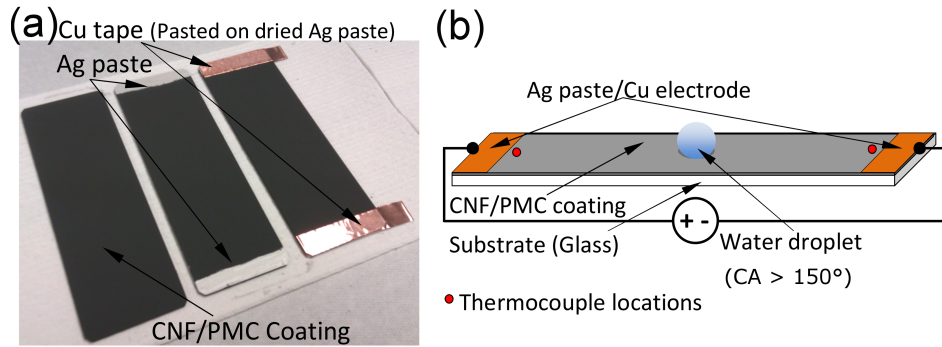


Figure 8. (a) Stepwise process of depositing electrodes on the dry CNF-PMC coating on glass slide (7.5×2.5 cm). (b) Schematic of the setup electrothermal characterization.

that the nanocomposite attains a minimal resistivity with increased coating thickness. No significant change in wettability was observed with the amount of coating deposited. Figure 9b shows linear I-V characteristics with varying DC voltage.

The temperature evolution of the coating with time for fixed input DC voltage in a closed environmental chamber (no forced circulation) is shown in Figure 9c. The temperature of the coating rose rapidly and attained a constant value after reaching thermal equilibrium with the surroundings. The equilibrium temperature depends on the input power, convective heat transfer coefficient (natural convection is present) and the cross-section area of the coating (i.e. its thickness, since the coating width is fixed). As expected and shown in Figure 9d, the steady state temperature increased linearly with input power density (W cm^{-2}). Previous studies on heating performance have established that the transient (or dynamic) response of a heater depends on the conductive losses between film and the substrate but, the steady state temperature attained for a given input power density is dictated by material- ambient

gas interactions quantified by the convective heat transfer coefficient [49, 50]. We evaluate the heat performance of the CNF film by the slope of the steady state temperature variation with input power density (Figure 9d). This temperature varied linearly with power density. Table 2 compares the heating performance of various CNT based heating systems. The heat performance value of $153 \text{ }^\circ\text{C cm}^{-2} \text{ W}^{-1}$ obtained herein is comparable to the values reported in previous studies that used nanocarbon based materials primarily to form much thinner films. Despite their micro/nano texture, which provides a larger area for convective heat losses, the present coatings perform well thermoelectrically.

TABLE II
COMPARISON OF THE HEATING PERFORMANCE OF NANOCARBON-BASED HEATERS FROM LITERATURE.

Material	Substrate	Heat performance $10^{-4}^\circ\text{C m}^2 \text{ W}^{-1}$	Method	Reference
SWCNT	glass	212	spray deposition	[49]
	glass	208	dip coating	[51]
CNF	glass	153	spray deposition	present
MWCNT/Pd ^a	free standing sheet	99	chemical vapor deposition	[50]
MWCNT	PET ^b	94	chemical vapor deposition	[52]
	free standing sheet	27	chemical vapor deposition	[50]

^athermally grown granular type palladium.

^bpolyethylene terephthalate.

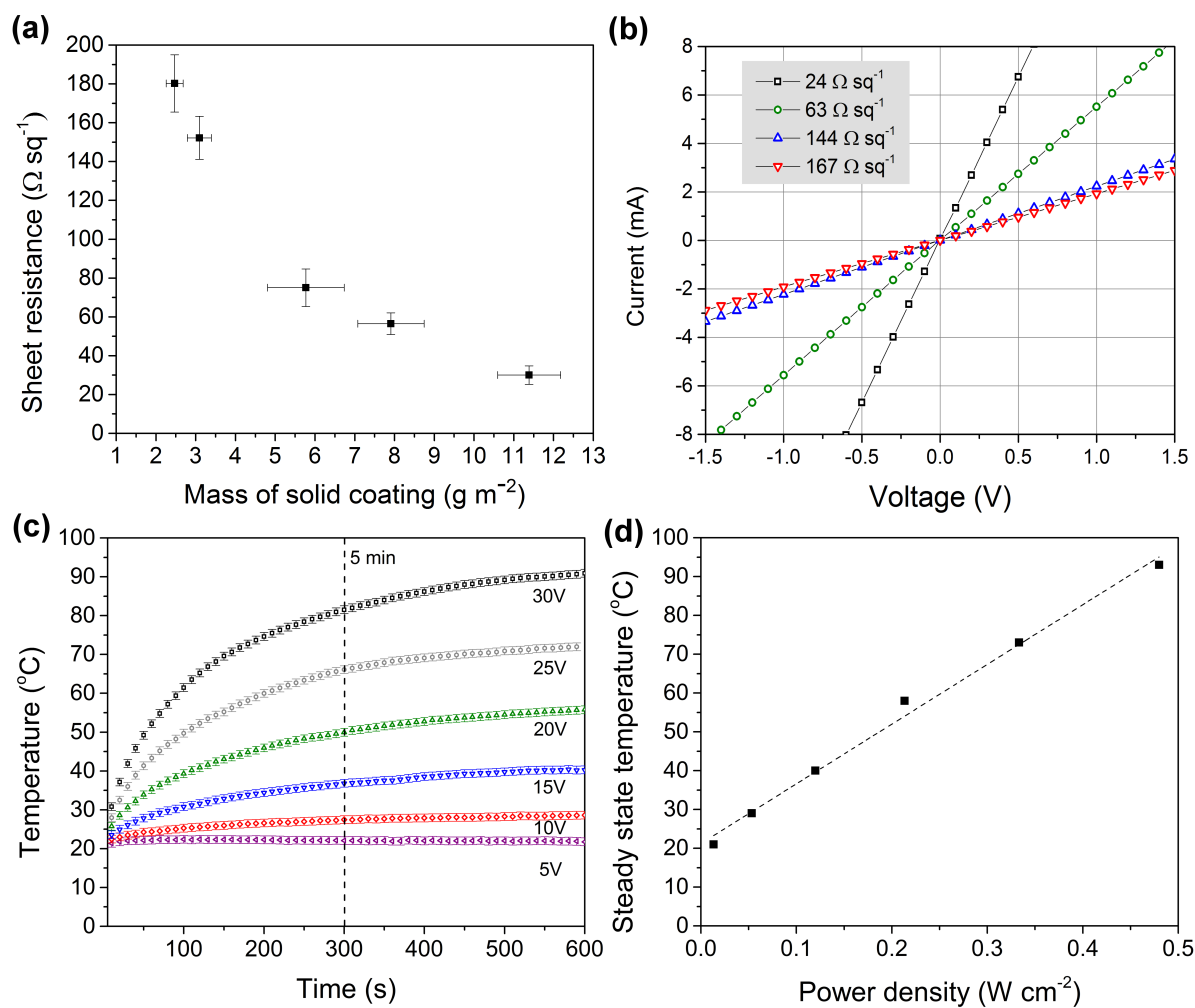


Figure 9. (a) Reduction in sheet resistance with amount of solid CNF-PMC coating deposited on the glass substrate. (b) I-V characteristics of the CNF-PMC coatings with varying sheet resistance (coating thickness). (c) Temperature evolution of a 110Ω CNF-PMC coating for various values of applied DC voltage. (d) Steady state temperature versus input power density for the same coating as in (c).

3.2.2 Condensation Frosting and Defrosting by Joule Heating

We study condensation frosting on the coating by gradually cooling the surface from the ambient temperature (T_a) of 15°C to $-10 \pm 1^\circ\text{C}$ under relative humidity of 80%. Low cooling rate ($\sim 3^\circ\text{C}/\text{min}$) is employed to ensure condensation as the dominant mode of phase change, followed by frosting. As previously demonstrated dropwise condensation on micro/nanostructured superhydrophobic coatings creates highly mobile micrometer size droplets. After the initial nucleation phase, the droplets coalesced to form larger droplets, and in that process, some gained enough energy to depart the surface. Figure 10 shows a sequence of such droplet jumping events. Droplet jumping is dictated by the micro/nano structure and the nucleation density; here we observed jumping from merging of a large cluster of droplets (each $< 50\mu\text{m}$ in diameter). Not all droplets departed from the surface and those that remained on the surface after further coalescence and growth eventually reached a supercooled state. Thereafter, supercooled droplets froze by a propagating freezing wave front that initiated at the edge of the sample. Freezing of the supercooled condensate on the superhydrophobic surface caused a sudden loss of both droplet mobility and transparency, as the droplets turned hazy due to crystallization. The frost preferentially grew outwards from the surface (Figure 11) forming a highly porous dendritic network. The frost thus formed on the surface was mostly in a Cassie state, called Cassie frost.

Using the above procedure, we let frost accumulate on an uncoated glass slide, and two identical CNF-PMC coatings, one of which was connected to a DC power source. These three samples are shown side-by-side in Figure 12, which depicts them in their frosted state. On

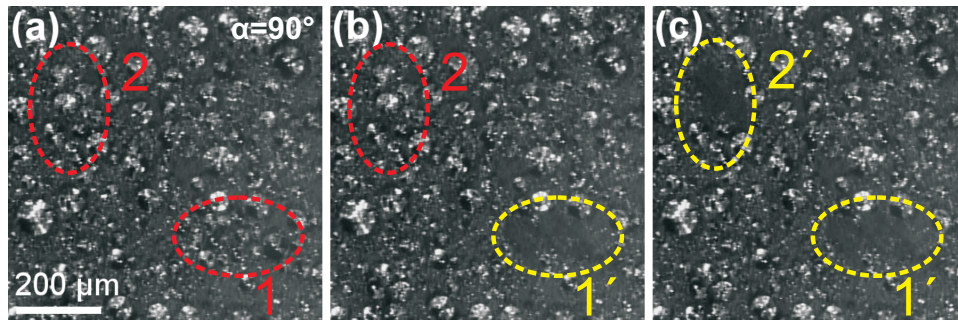


Figure 10. Image sequence showing out-of-plane droplet jumping. Two clusters of droplets below $50\mu\text{m}$ are encircled in red in (a) in their pre-coalescence state (1,2). In (b), the droplets in the red area are still distinct (2), while those in the yellow area have coalesced and departed out of the surface leaving behind pristine sites for fresh nucleation to occur thereby (1'). In (c), both areas are devoid of droplets and start a new cycle of liquid nucleation (1',2').

the glass slide, the condensate froze immediately after the temperature declined below 0°C . As expected, both coatings frosted simultaneously showing no difference in frosting delay and frost morphology compared to each other. To activate skin heating, a constant DC voltage of 40V (power density of 0.77 Wcm^{-2}) was applied across the active coating till the surface became completely frost free. The peltier cooling was active during this entire procedure to eliminate any heating from underneath the coating; this also required the application of relatively large voltage (40V) to overpower the heat drained by the peltier stage.

The phenomenon of defrosting was studied in further detail by viewing a smaller area ($8.5 \times 8.5\text{ mm}$); see sequence in Figure 13. Frost was accumulated for an hour from when the sample was cooled to $-10 \pm 1^\circ\text{C}$ under high humidity conditions (ambient temperature of 15°C and RH of 80%). Constant DC voltage of 40V (power density of 0.77 W cm^{-2}) was applied and the

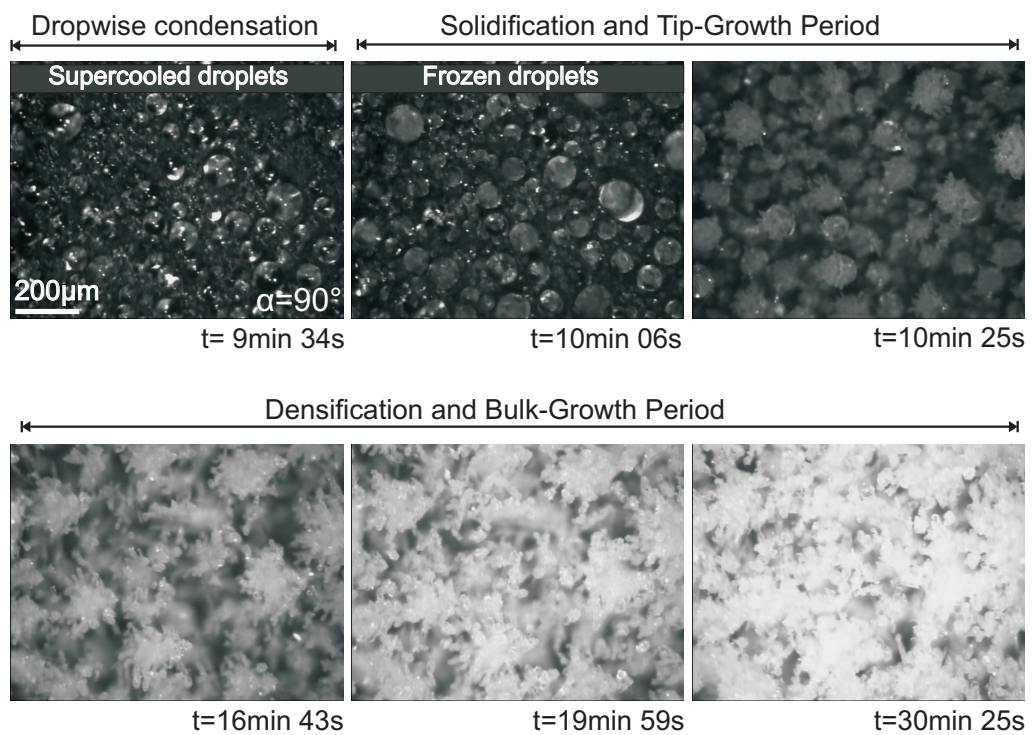


Figure 11. Stages of frost growth. The condensed supercooled droplets froze, frost preferentially grew on the tip of the droplets forming a porous dendritic structure.

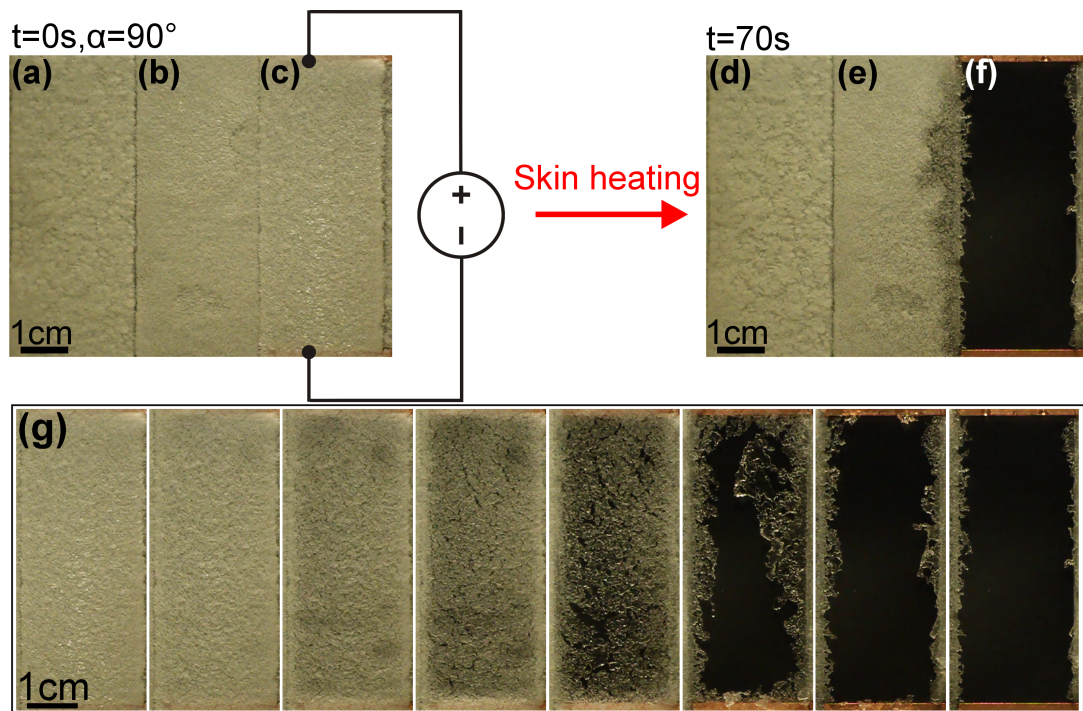


Figure 12. Surfaces (a) glass slide, (b) 50 wt.% CNF coating and (c) 50 wt.% CNF coating with joule heating after exposure to humid ambient (15°C and $\text{RH} = 80\%$) for 1 hour. Surfaces (d) glass slide and (e) 50 wt.% CNF coating still covered with frost and (f) 50 wt.% CNF completely frost free after application of 40V DC for 70s. (g) Sequence of images showing rapid transition of frosted coating (c) to completely ice free surface (f) by joule heating. Each image in sequence (g) is captured 10s apart.

temperature of the coating was recorded in real time until complete defrosting. We observed that the thick layer of frost started to melt from above (ambient side) and below (coating side). This was confirmed by viewing the defrosting process sideways. The continuous layer of the frost fractured, while the melted water wicked and spread in the porous hydrophilic frost layer above, to form solid-liquid slush. Most of this slush maintained the form of a sheet that separated from the surface making it mobile, except for few anchor points along the edges of the coating. The slush sheet then curled away or detached and slid off (as $\alpha=90^\circ$) the surface, leaving the coating frost free. The temperature of the coating was measured to be $\sim 2^\circ\text{C}$, just above the melting point. Complete defrosting at low temperatures (around 0°C) is highly desired as it would save time and cost needed for deicing in sub-zero conditions where there is no heating of the frost layer from the ambient side.

In situations where external forces are unavailable to aid defrosting (e.g., wind shear, gravity etc.), the surface property must promote facile dewetting. Figure 14 shows dynamics of the defrosting at an inclination angle of 10° . The frozen Cassie condensate melts, and this melt wicks into the porous frost forming a partially melted sheet. It is interesting to note that the sheet of solid-liquid slush was seen to curl away from the coating at low inclination angles. Further, the partially melted frost completely dewets the coating, thus forming mobile droplets which roll away [9]. The micro/nano hierarchical structure energetically favors complete dewetting during the phase change process and aids liquid mobility [22]. The last three images of the sequence in Figure 14 demonstrate the ability of the coating to regain its superhydrophobicity while still maintaining its self cleaning ability. The capability of the present coating to completely defrost

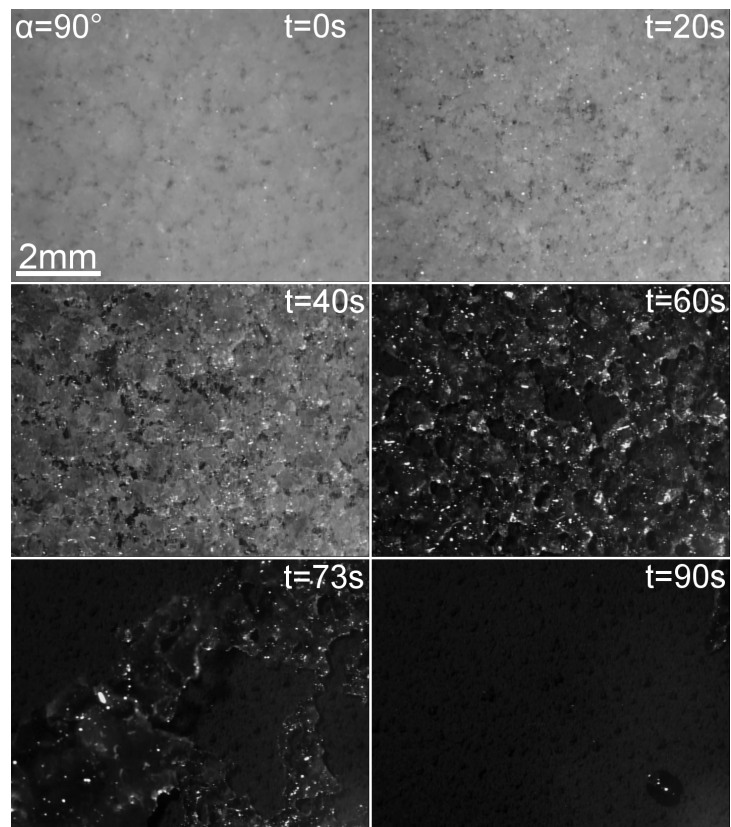


Figure 13. Top view of dynamic defrosting by skin heating. A constant DC voltage of 40V was applied to the coating till the coating became frost free. The temperature of the coating rose from -10°C to just above melting point ($\sim 2^\circ\text{C}$), eventually leaving a frost-free surface.

Time was set to zero from the point of application of the voltage.

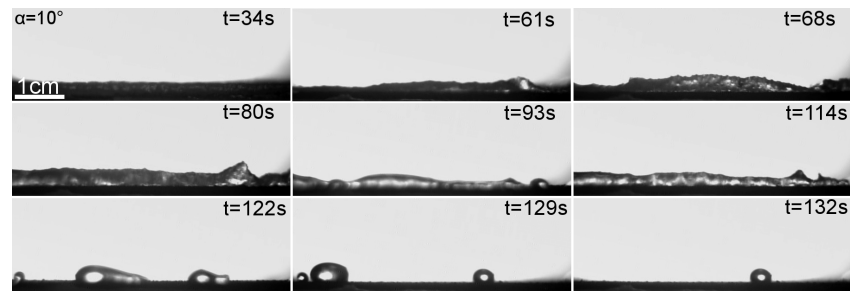


Figure 14. Side view images showing dynamic defrosting at low angle of inclination of $\alpha = 10^\circ$ in humid environment (ambient temperature of 15°C and RH of 80%).

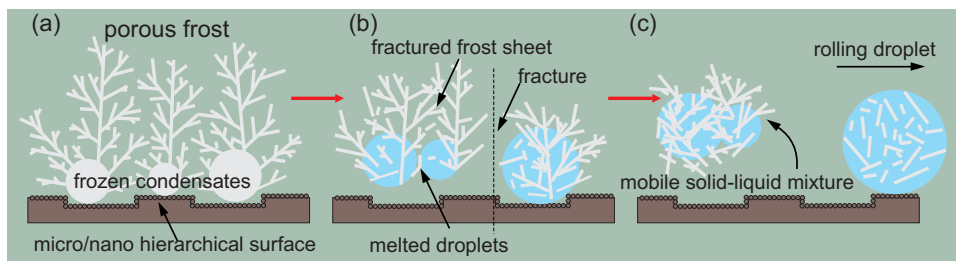


Figure 15. Illustration of dynamic defrosting. (a) Porous frost formed on the frozen condensates in a Cassie state, (b) Melted droplets absorbed by the porous medium. The frost layer fractures carrying partially melted solid-liquid mixture. (c) The sheet of solid-liquid mixture either curls away or forms a droplet that rolls away leaving a frost-free surface.

without the need of large external force is extremely desirable as a standalone system to address ice mitigation.

CHAPTER 4

CONCLUSION

A simple, scalable and low-cost technique is presented to cast carbon nanofiber based superhydrophobic coating for anti-icing/anti-frosting applications. Firstly, the wettability of CNF-PMC based nanocomposite was tuned by varying the filler concentration. A sudden transition from sticky hydrophobic to superhydrophobic and self-cleaning surface occurred at 30 wt.% filler loading. An optimal nanocomposite composition (50 wt.% CNF loading) was identified to ensure sustained DWC showing nucleation, growth and shedding cycle. Nanoscale features governed the condensed micro-droplet morphology. Suspended droplet morphology was identified to be highly desirable, showing suppressed droplet growth, while maintaining high droplet mobility.

In conclusion, for the first time, dynamic defrosting was demonstrated on carbon nanofiber based polymeric film that facilitate skin heating. Distribution of smaller droplets in a suspended state lead to weak anchor points for the frost formed on a cold surface exposed to a humidity-rich ambient. The low surface area covered by the drops provides low adhesion of the highly porous frost layer formed on the repellent surface. When heated from underneath, the frost anchoring points first melt to be absorbed by the hydrophilic porous medium built above it. Low surface wettability aided by the wicking of the liquid into the porous frost help the liquid slush to completely dewet the heated surface. The partially melted frost layer thus released from the surface shrinks due to the energetically driven reduction in surface area of this mixed medium. The frost layer curls away from the surface, further assisting dewetting, finally

leaving behind a completely dry surface when the floating slush volumes slide off. The heating performance of coatings compared well with the other existing nanocarbon based heaters. Thus, facile defrosting enabled by micro/nanotextured, self-heated, superhydrophobic surfaces shows promise to the icing problem. An advantage of joule heating of the superhydrophobic film is that it eliminates the need for any external source of heating element/system, reducing cost, space and weight. Optimized pulsing of voltage and smart re-routing of leak-current can further reduce energy consumption during de-icing.

CITED LITERATURE

1. Yao, Y., Jiang, Y. Q., Deng, S. M., and Ma, Z. L.: A study on the performance of the air-side heat exchanger under frosting in an air source heat pump water heater/chiller unit. International Journal of Heat and Mass Transfer, 47(17-18):3745–3756, August 2004.
2. Parent, O. and Ilinca, A.: Anti-icing and de-icing techniques for wind turbines: Critical review. Cold Regions Science and Technology, 65(1):88–96, January 2011.
3. Gent, R., Dart, N., Cansdale, J., Gent, R., Dart, N., and Cansdale, J.: Aircraft icing. Philosophical Transactions of the Royal Society of London. Series A: Mathematical, Physical and Engineering Sciences, 358(1776):2873–2911, 2000.
4. Laforte, J. L., Allaire, M. A., and Laflamme, J.: State-of-the-art on power line de-icing. Atmospheric Research, 46(1-2):143–158, April 1998.
5. Ryerson, C. C.: Ice protection of offshore platforms. Cold Regions Science and Technology, 65(1):97–110, January 2011.
6. Yamauchi, G., Takai, K., and Saito, H.: Ptfе based water repellent coating for telecommunication antennas. IEICE Transactions on Electronics, 83(7):1139–1141, 2000.
7. Boinovich, L. B. and Emelyanenko, A. M.: Anti-icing potential of superhydrophobic coatings. Mendelev Communications, 23(1):3–10, 2013.
8. Tourkine, P., Le Merrer, M., and Qué ré, D.: Delayed freezing on water repellent materials. Langmuir, 25(13):7214–7216, 2009.
9. Boreyko, J. B., Srijanto, B. R., Nguyen, T. D., Vega, C., Fuentes-Cabrera, M., and Collier, C. P.: Dynamic defrosting on nanostructured superhydrophobic surfaces. Langmuir, 29(30):9516–9524, July 2013.
10. Cao, L., Jones, A. K., Sikka, V. K., Wu, J., and Gao, D.: Anti-icing superhydrophobic coatings. Langmuir, 25(21):12444–12448, 2009.

11. Mishchenko, L., Hatton, B., Bahadur, V., Taylor, J. A., Krupenkin, T., and Aizenberg, J.: Design of ice-free nanostructured surfaces based on repulsion of impacting water droplets. ACS nano, 4(12):7699–7707, 2010.
12. Jung, S., Dorrestijn, M., Raps, D., Das, A., Megaridis, C. M., Poulikakos, D., et al.: Are superhydrophobic surfaces best for icephobicity? Langmuir, 27(6):3059, 2011.
13. Varanasi, K. K., Deng, T., Smith, J. D., Hsu, M., and Bhate, N.: Frost formation and ice adhesion on superhydrophobic surfaces. Applied Physics Letters, 97:234102, 2010.
14. Yeong, Y. H., Steele, A., Loth, E., Bayer, I., De Combarieu, G., and Lakeman, C.: Temperature and humidity effects on superhydrophobicity of nanocomposite coatings. Applied Physics Letters, 100(5):053112, January 2012.
15. Chen, J., Liu, J., He, M., Li, K., Cui, D., Zhang, Q., Zeng, X., Zhang, Y., Wang, J., and Song, Y.: Superhydrophobic surfaces cannot reduce ice adhesion. Applied Physics Letters, 101(11):111603–111603, 2012.
16. Smith, J. D., Dhiman, R., Anand, S., Reza-Garduno, E., Cohen, R. E., McKinley, G. H., and Varanasi, K. K.: Droplet mobility on lubricant-impregnated surfaces. Soft Matter, 9(6):1772–1780, 2013.
17. Rykaczewski, K., Anand, S., Subramanyam, S. B., and Varanasi, K. K.: Mechanism of frost formation on lubricant-impregnated surfaces. Langmuir, 29(17):5230–5238, April 2013.
18. Jung, S., Tiwari, M. K., Doan, N. V., and Poulikakos, D.: Mechanism of supercooled droplet freezing on surfaces. Nature Communications, 3:615, 2012.
19. Jung, S., Tiwari, M. K., and Poulikakos, D.: Frost halos from supercooled water droplets. Proceedings of the National Academy of Sciences of the United States of America, 109(40):16073–16078, October 2012.
20. Na, B. and Webb, R. L.: A fundamental understanding of factors affecting frost nucleation. International Journal of Heat and Mass Transfer, 46(20):3797–3808, September 2003.
21. Jing, T., Kim, Y., Lee, S., Kim, D., Kim, J., and Hwang, W.: Frosting and defrosting on rigid superhydrophobic surface. Applied Surface Science, 276:37–42, July 2013.

22. Chen, X., Ma, R., Zhou, H., Zhou, X., Che, L., Yao, S., and Wang, Z.: Activating the microscale edge effect in a hierarchical surface for frosting suppression and defrosting promotion. Scientific reports, 3, 2013.
23. Antonini, C., Innocenti, M., Horn, T., Marengo, M., and Amirfazli, A.: Understanding the effect of superhydrophobic coatings on energy reduction in anti-icing systems. Cold Regions Science and Technology, 67(1):58–67, 2011.
24. Das, A., Schutzius, T. M., Bayer, I. S., and Megaridis, C. M.: Superoleophobic and conductive carbon nanofiber/fluoropolymer composite films. Carbon, 50(3):1346–1354, March 2012.
25. De Gennes, P.-G., Brochard-Wyart, F., and Quéré, D.: Capillarity and wetting phenomena: drops, bubbles, pearls, waves. Springer, 2004.
26. Wenzel, R. N.: Resistance of solid surfaces to wetting by water. Ind. Eng. Chem., 28(8):988–994, August 1936.
27. Cassie, A. B. D. and Baxter, S.: Wettability of porous surfaces. Trans. Faraday Soc., 40(0):546–551, 1944.
28. Kim, P., Wong, T.-S., Alvarenga, J., Kreder, M. J., Adorno-Martinez, W. E., and Aizenberg, J.: Liquid-infused nanostructured surfaces with extreme anti-ice and anti-frost performance. Acs Nano, 6(8):6569–6577, August 2012.
29. Rykaczewski, K., Osborn, W. A., Chinn, J., Walker, M. L., Scott, J. H. J., Jones, W., Hao, C., Yao, S., and Wang, Z.: How nanorough is rough enough to make a surface superhydrophobic during water condensation? Soft Matter, 8(33):8786–8794, 2012.
30. Rose, J. W.: Condensation heat transfer fundamentals. Chemical Engineering Research & Design, 76(A2):143–152, February 1998.
31. Miljkovic, N., Enright, R., Nam, Y., Lopez, K., Dou, N., Sack, J., and Wang, E. N.: Jumping-droplet-enhanced condensation on scalable superhydrophobic nanostructured surfaces. Nano Letters, 13(1):179–187, January 2013.
32. Miljkovic, N. and Wang, E. N.: Condensation heat transfer on superhydrophobic surfaces. MRS Bulletin, 38(5):397–406, May 2013.

33. Rykaczewski, K., Paxson, A. T., Anand, S., Chen, X., Wang, Z., and Varanasit, K. K.: Multimode multidrop serial coalescence effects during condensation on hierarchical superhydrophobic surfaces. Langmuir, 29(3):881–891, January 2013.
34. Cheng, J., Vandadi, A., and Chen, C.-L.: Condensation heat transfer on two-tier superhydrophobic surfaces. Applied Physics Letters, 101(13):131909, September 2012.
35. Boreyko, J. B. and Chen, C.-H.: Self-propelled dropwise condensate on superhydrophobic surfaces. Physical Review Letters, 103(18):184501, October 2009.
36. Chen, C.-H., Cai, Q., Tsai, C., Chen, C.-L., Xiong, G., Yu, Y., and Ren, Z.: Dropwise condensation on superhydrophobic surfaces with two-tier roughness. Applied Physics Letters, 90(17):173108, April 2007.
37. Enright, R., Miljkovic, N., Al-Obeidi, A., Thompson, C. V., and Wang, E. N.: Condensation on superhydrophobic surfaces: The role of local energy barriers and structure length scale. Langmuir, 28(40):14424–14432, 2012.
38. Liu, T., Sun, W., Sun, X., and Ai, H.: Thermodynamic analysis of the effect of the hierarchical architecture of a superhydrophobic surface on a condensed drop state. Langmuir, 26(18):14835–14841, September 2010.
39. Miljkovic, N., Enright, R., and Wang, E. N.: Effect of droplet morphology on growth dynamics and heat transfer during condensation on superhydrophobic nanostructured surfaces. ACS Nano, 6(2):1776–1785, February 2012.
40. Tuteja, A., Choi, W., McKinley, G. H., Cohen, R. E., and Rubner, M. F.: Design parameters for superhydrophobicity and superoleophobicity. MRS Bulletin, 33:752–758, 7 2008.
41. Schutzius, T. M., Elsharkawy, M., Tiwari, M. K., and Megaridis, C. M.: Surface tension confined (stc) tracks for capillary-driven transport of low surface tension liquids. Lab on a Chip, 12(24):5237–5242, 2012.
42. Dorrer, C. and Ruehe, J.: Condensation and wetting transitions on microstructured ultrahydrophobic surfaces. Langmuir, 23(7):3820–3824, March 2007.
43. Fletcher, N.: Size effect in heterogeneous nucleation. The Journal of chemical physics, 29:572, 1958.

44. Liu, Z., Gou, Y., Wang, J., and Cheng, S.: Frost formation on a super-hydrophobic surface under natural convection conditions. International Journal of Heat and Mass Transfer, 51(25-26):5975–5982, December 2008.
45. He, M., Wang, J., Li, H., Jin, X., Wang, J., Liu, B., and Song, Y.: Super-hydrophobic film retards frost formation. Soft Matter, 6(11):2396–2399, 2010.
46. He, M., Wang, J., Li, H., and Song, Y.: Super-hydrophobic surfaces to condensed microdroplets at temperatures below the freezing point retard ice/frost formation. Soft Matter, 7(8):3993–4000, 2011.
47. Boreyko, J. B. and Collier, C. P.: Delayed frost growth on jumping-drop superhydrophobic surfaces. ACS Nano, 7(2):1618–1627, 2013.
48. Al-Saleh, M. H. and Sundararaj, U.: A review of vapor grown carbon nanofiber/polymer conductive composites. Carbon, 47(1):2–22, January 2009.
49. Bae, J. J., Lim, S. C., Han, G. H., Jo, Y. W., Doung, D. L., Kim, E. S., Chae, S. J., Huy, T. Q., Luan, N. V., and Lee, Y. H.: Heat dissipation of transparent graphene defoggers. Adv. Funct. Mater., 22(22):4819–4826, November 2012.
50. Im, H., Jang, E. Y., Choi, A., Kim, W. J., Kang, T. J., Park, Y. W., and Kim, Y. H.: Enhancement of heating performance of carbon nanotube sheet with granular metal. ACS Applied Materials & Interfaces, 4(5):2338–2342, May 2012.
51. Kang, T. J., Kim, T., Seo, S. M., Park, Y. J., and Kim, Y. H.: Thickness-dependent thermal resistance of a transparent glass heater with a single-walled carbon nanotube coating. Carbon, 49(4):1087 – 1093, 2011.
52. Jang, H.-S., Jeon, S. K., and Nahm, S. H.: The manufacture of a transparent film heater by spinning multi-walled carbon nanotubes. Carbon, 49(1):111–116, January 2011.

VITA

NAME

Shreyas Kapatral

EDUCATION

B.Tech., Mechanical Engineering, National Institute of Technology, Rourkela, India, 2008

M.S., Mechanical Engineering, University of Illinois at Chicago, Expected 2013

TEACHING EXPERIENCE

Teaching Assistant (TA), Introduction to Thermodynamics (ME 205), University of Illinois at Chicago, Fall 2013, Spring 2012

Teaching Assistant (TA), Fluid Mechanics (ME 211), University of Illinois at Chicago, Fall 2012, Spring 2013

PROFESSIONAL EXPERIENCE

Development Engineer, Bosch Limited, Bengaluru, India. (2010-2011)

Project Assistant, Mechanical Engineering, Indian Institute of Science, Bengaluru, India. (2009-2010)

Design Engineer, General Electric Limited, Bengaluru, India. (2008-2009)

PUBLICATIONS

S. Kapatral, A. Das, C. M. Megaridis, "Large-Area Polymer-Composite Su-

per Liquid Repellent Coatings for On-Demand Anti-Icing/Frosting Control,”
in preparation

DISCLOSURE

C. M. Megaridis, T. Schutzius, S. Kapatral, A. Gosh. *Wettability Line-Patterned Surfaces for Enhanced Water Condensation Rates from Humid Gas Atmospheres*.
Invention Disclosure DG123 (filed on 3-27-2013).